

Wavelet Analysis of Rotor-Tip Disturbances in an Axial-Flow Compressor

Feng Lin*

Indiana Institute of Technology, Fort Wayne, Indiana 46803

and

Jingyi Chen[†] and Meilin Li[‡]

Chinese Academy of Sciences, 100080 Beijing, People's Republic of China

Dynamic pressure signals taken from a low-speed axial compressor are analyzed with a wavelet transform. Several practical issues of continuous wavelet transforms, within the context of rotor-tip flow analysis, are discussed. The discrete form of continuous wavelet transform is presented with a graphical derivation that uniquely explains a complicated mathematical process with a readable graphical language without losing much mathematical strictness. With this wavelet tool, the data from a low-speed, three-stage axial compressor are analyzed. In these data, the wavelet analysis is able to pinpoint the exact time when spikes were initiated, as early as hundreds of rotor revolutions prior to stall, and track them thereafter. It is found that the emergence of the spikes is strongly related to two structural asymmetries of this compressor, one in the rotating frame and the other in the stationary frame. The spike development is not continuous. The ability to track the prestall process in both time and space, as demonstrated in this paper, makes wavelet analysis an effective tool for investigating the complicated instability phenomena of axial compressors.

Nomenclature

E	=	wavelet spectral energy density
\mathcal{F}^{-1}	=	inverse Fourier transform
f_{rot}	=	rotor frequency
f_0	=	$1/T_0$
f_1	=	Nf_0
$H(\omega)$	=	heaviside step function; equal to 1 if $\omega > 0$, 0 otherwise
N	=	total number of samples
s	=	scale
T	=	sampling period
T_0	=	total sampling time, $T_0 = NT$
t, τ	=	time
WX	=	wavelet transform of x
X, Y, \dots	=	Fourier transform of x, y, \dots
x, y, \dots	=	time series
δ	=	delta function
ψ, Ψ	=	mother wavelet or wavelet base and its Fourier transform
ψ^*	=	complex conjugate of ψ

I. Introduction

THE instability of compression systems, whose basic modes are rotating stall and surge, is a long-standing problem of turbomachinery. It continues to attract a great deal of attention of researchers from a variety of disciplines, such as fluid mechanics, nonlinear dynamics, controls, high-speed measurements, and signal processing. One of the recent interests is to investigate how the instability is triggered and how the system parameters affect the triggering process.

Understanding this triggering mechanism is vital to the development of both active control and operability enhancement of the compression systems. It will also help designers to design compressors that are more robust to flow disturbances.

The flow disturbances that appear before fully developed rotating stall play an important role in stall development, and some are believed to trigger stall. The disturbances that actually trigger the system instability are called stall precursors. The past 10 years of research have demonstrated that “modes” and “spikes” are two basic types of stall precursors.^{1,2} A number of studies have been carried out to understand the flow structure and dynamic response of modes and spikes.^{3–5} Although the stall precursors exist in the pressure or velocity signals obtained from sensors in the tip region of rotor blades, it is difficult to identify them because they are embedded within the blade passage flows and measurement noise, especially in their early stage of development. To unveil the instability mechanism in compressors, it is crucial to first have the ability to detect and track all of the rotating flow disturbances that appear in the prestall stage. The stall precursors can then be extracted from these disturbances. For modal stall precursors, Tryfonidis et al.⁶ developed a method to detect such modal waves by tracking traveling wave energy. The signal processing for spikes is much more complex because of their unsteadiness and nonlinearity. Bright et al.⁷ and Lin⁸ applied different techniques of nonlinear time series analysis to this problem.

The wavelet transform appears to be a natural choice for investigating prestall flow disturbances and detecting stall precursors^{9–13} because of its time-frequency analysis ability that is ideal for analyzing unsteady signals. Liao and Chen⁹ used a continuous wavelet to first perform the time-frequency analysis of stall inception, in which the focus was on the time derivative of the phase. Cheng¹⁰ applied wavelet-based image-processing techniques to two-dimensional images that were constructed from the pressure signal. He extracted the features of the images at different time scales. The approach of Le et al.¹¹ was a multiscale analysis using a compact-harmonic, Mexican-hat-shaped wavelet filter bank. Inoue et al.¹² chose a spiky-shaped continuous wavelet and applied it to low-pass filtered data. They treated the small- and the large-scale bands independently as if they were produced by independent short and large-scale waves. Höss et al.¹³ used a discrete wavelet transform and a statistical evaluation of the amplitude variation for the throttling processes in their tests.

Received 15 October 2002; revision received 24 September 2003; accepted for publication 15 October 2003. Copyright © 2004 by the authors. Published by the American Institute of Aeronautics and Astronautics, Inc., with permission. Copies of this paper may be made for personal or internal use, on condition that the copier pay the \$10.00 per-copy fee to the Copyright Clearance Center, Inc., 222 Rosewood Drive, Danvers, MA 01923; include the code 0748-4658/04 \$10.00 in correspondence with the CCC.

*Associate Professor, Department of Mechanical Engineering; lin@indtech.edu. Senior Member AIAA.

[†]Professor, Institute of Engineering Thermophysics; cji@mail.etp.ac.cn.

[‡]Research Assistant, Institute of Engineering Thermophysics; lml@mail.etp.ac.cn.

Despite all of the aforementioned progress in stall precursor research, the ability to provide clear, first-hand pictures of the emergence and development of spikes is still lacking. It is not uncommon for wavelet users to feel that the relationship between the wavelet spectra and the spike characteristics is somewhat ambiguous. There are many practical issues that need to be resolved, such as the choice of the wavelet bases, the choices of the set of discrete scales and time for performing a continuous wavelet transform computationally, and the edge effect. Inappropriate choices can prevent the features of the signal from being identified, or, even worse, an incorrect conclusion could result in a “false positive.” Thus, Secs. II and III provide practical guidelines to configure the wavelet properly within the context of rotor-tip flow analysis. To this end, a unique graphical derivation of the discrete form of an one-dimensional continuous wavelet transform is used as a tool to resolve the practical issues. Section IV defines the time-averaged and scale-averaged wavelet spectra for later use. Sections V–VII are concerned with the application of the wavelet transform to the experimental test data taken from a low-speed three-stage axial compressor. The patterns on the wavelet spectrum are directly linked to the characteristics of rotating disturbances. The exact location and time where a spike is initiated can be pinpointed, and its growth or decay can be tracked. One rotating and one stationary asymmetry in the flow structure of this compressor are identified, and their role in triggering spikes is explored. Finally the paper ends with discussions and conclusions in Secs. VIII and IX.

II. One-Dimensional, Continuous Wavelet Transform

Definition of Wavelet Transform

A one-dimensional, continuous wavelet transform is defined as

$$WX(s, t) = \frac{1}{\sqrt{|s|}} \int_{-\infty}^{\infty} x(\tau) \psi^* \left(\frac{\tau - t}{s} \right) d\tau \quad (1)$$

The factor $1/\sqrt{|s|}$ is introduced to keep the energy the same for the wavelet base with various scales s because

$$\begin{aligned} \int_{-\infty}^{\infty} \left| \frac{1}{\sqrt{|s|}} \psi \left(\frac{\tau}{s} \right) \right|^2 d\tau &= \int_{-\infty}^{\infty} \left| \psi \left(\frac{\tau}{s} \right) \right|^2 d \left(\frac{\tau}{s} \right) \\ &= \int_{-\infty}^{\infty} |\psi(u)|^2 du \end{aligned}$$

This makes the wavelet spectral energy density at various scales comparable. Because negative s does not have physical meaning, we will simply use s for $|s|$ in the rest of this paper. It can be shown that

$$WX(s, t) = \sqrt{s} \{ \mathcal{F}^{-1} [X(\omega) \Psi(s\omega)] \}_t \quad (2)$$

This equation shows that a one-dimensional continuous wavelet transform is equivalent to a bank of bandpass filters with dilated and translated windows. Hence, Fourier-transform-based filtering is not necessary prior to wavelet transform.

The Parseval formula

$$\int_{-\infty}^{\infty} |x(t)|^2 dt = \int_{-\infty}^{\infty} \int_0^{\infty} \frac{|WX(s, t)|^2}{\pi} ds dt$$

states that $E = |WX(s, t)|^2$ can be interpreted as spectral energy density at scale s and time t . The map of E as function of s and t is the wavelet spectrogram.

We use an example here to illustrate how a continuous wavelet transform is obtained. Consider a pure sinusoidal signal $x(\tau) = a \exp(i\beta\tau) + c.c.$, where $c.c.$ is the acronym for complex conjugate. When using the Morlet wavelet (Table 1) as the mother wavelet, its transform is

$$WX(s, t) = 2\pi^{\frac{3}{4}} a \sqrt{s} \mathcal{F}^{-1} [\delta(\omega - \beta) H(\omega) e^{-(s\omega - \omega_0)^2/2}]$$

after considering the fact that the Fourier transform of $e^{-i\beta\tau}$ is $2\pi\delta(\omega - \beta)$. Figure 1 illustrates the shapes and locations of

Table 1 Wavelet base functions taken from Torrence and Compo¹⁴ (The wavelet bases are normalized so that $\int_{-\infty}^{\infty} |\Psi_0(s\omega)|^2 d\omega = 1$.)

Name	$\psi_0(\eta)$	$\Psi_0(s\omega)$
Morlet	$\frac{1}{\pi^{\frac{1}{4}}} e^{i\omega_0\eta} e^{-\eta^2/2}$	$\frac{1}{\pi^{\frac{1}{4}}} H(\omega) e^{-(s\omega - \omega_0)^2/2}$
DOG ^a	$\frac{(-1)^{m+1}}{\sqrt{\Gamma(m + \frac{1}{2})}} \frac{d^m}{d\eta^m} (e^{-\eta^2/2})$	$\frac{-i^m (s\omega)^m}{\sqrt{\Gamma(m + \frac{1}{2})}} [e^{-(s\omega)^2/2}]$

^aDOG = derivative of Gaussian. When $m = 2$, it is the Mexican hat wavelet.

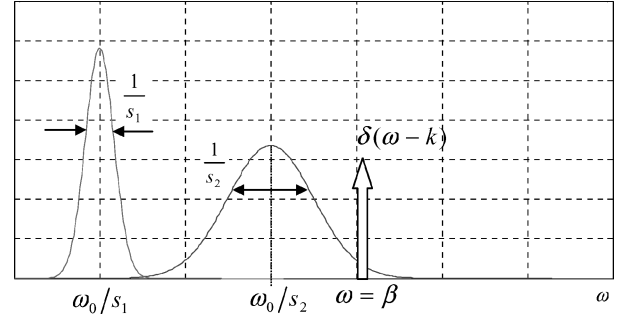


Fig. 1 Illustration of the shape and the location of the Morlet wavelet and their relation with $\delta(\omega - \beta)$ as the scales vary: $s_1 > s_2$.

Gaussian-like function $\sqrt{s} e^{-(s\omega - \omega_0)^2/2}$ at small and large scales and their relation with $\delta(\omega - \beta)$. One can see from this figure that the wavelet coefficients are negligibly small when β is far away from the center of the Gaussian curve and reach a maximum when β is close to ω_0/s . So, there exists a one-to-one correspondence between the wavelet scale s and the Fourier period T . By directly integrating Eq. (1) and taking the derivative with respect to s , it can be shown that¹⁴

$$T = \frac{2\pi}{\beta} = \frac{4\pi s}{\omega_0 + \sqrt{\omega_0^2 + 2}}$$

The signal $x(\tau)$ can be reconstructed from the wavelet transform $WX(s, t)$.

$$x(\tau) = \frac{1}{C_\psi} \int_{-\infty}^{\infty} \int_{-\infty}^{\infty} [WX(s, t)] \psi_{s,t}(\tau) \frac{ds}{s^2} dt$$

where

$$C_\psi = \int_{-\infty}^{\infty} |\Psi(\omega)|^2 / |\omega| d\omega < \infty$$

Choice of Wavelet Base

To be called a wavelet base, a function $\psi(\tau)$ has to be admissible.¹⁵ That is, $\psi(\tau)$ must satisfy

$$\int_{-\infty}^{\infty} |\psi(\tau)| d\tau < \infty$$

and have a zero mean. Two groups of commonly used continuous wavelets, the Morlet wavelet and the derivative of a Gaussian (DOG), are listed in Table 1. Unlike the Fourier transform whose basis is always orthogonal, the choice of wavelet base is more versatile. For the same time series, different wavelet bases can lead to spectra that look completely different from each other. Therefore, the choice of wavelet base is crucial to wavelet analysis. Although experience plays an important role in the selection process, guidelines are provided, as follows, for the application to rotor-tip flows.

Orthogonal or Nonorthogonal

When applying wavelets to analyze the pressure signals from rotor-tip flows, orthogonal wavelets are not suitable for locating the rotating disturbances and tracking their development because

orthogonal wavelets are discrete in both time and scale. The discrete t axis might skip important instances of rotating disturbances. For this reason, we do not use orthogonal wavelets in this paper.

Real or Complex

For oscillatory signals, such as rotating disturbances in rotor-tip flows, a complex-valued wavelet is preferable to a real-valued wavelet. Complex-valued wavelets are suitable for capturing frequency and phase information. Real-valued wavelets are good for applications where the identification of peaks and singularities is the highest priority.

Shape and Resolution

It is argued by many authors that the shape of a wavelet base should reflect the type of features presented in the time series.^{14,15} However, this guideline can be misleading when applied to rotor-tip flows. The appropriate choice for rotor-tip flows should rely on the balance of resolutions in both the time and frequency domain. To identify rotating tip disturbances, we need a fine resolution on the time axis, so that we can locate the disturbances as small as a few blade passages in extent. At the same time, we need accurate information about the frequency, which is related to the reciprocal of the scale, so that we can determine the rotating speed of the disturbances. These two requirements contradict each other, and so a compromise must be made. A class of real-valued wavelet functions, such as DOGs, has high temporal resolution but very poor frequency resolution. This class of functions is therefore not a suitable choice. In this paper, the Morlet wavelet is chosen with $\omega_0 = 6$. Although it is not an optimal choice, it is reasonable for this application because its frequency and temporal resolutions are both sufficient.

III. Discrete Form of Continuous Wavelet Transform

To implement continuous wavelet transforms (CWT) computationally, one has to deal with discrete data series and discrete wavelet bases. In this section, we will graphically derive the discrete form of a CWT (DCWT). The DCWT is different from the discrete wavelet transform (DWT) because the DWT is used in the wavelet world to specifically refer to discrete form of wavelet transforms with orthogonal basis.

The digital implementation of the CWT can be obtained by numerically integrating Eq. (1) or by using the fast Fourier transform (FFT) on Eq. (2). The latter is much more popular because of the speed, accuracy, and efficiency of the FFT. The procedure is simple and straightforward. First, the FFT routine is used to obtain the discrete Fourier transform (DFT) $X(k)$ of measured time series $x(n)$, $n = 0, 1, \dots, N-1$:

$$X(k) = \sum_{n=0}^{N-1} x(n) e^{-i2\pi kn/N}$$

For a set of discrete scales, the Fourier spectra of the wavelet base is sampled in the same way as $X(k)$. The result is $\Psi(s_r \omega_k)$, $\omega_k = 2\pi k/NT$. Finally, the wavelet transform is the inverse DFT of $X(k)\Psi(s_r \omega_k)$:

$$W X_n(s_r) = \frac{\sqrt{s_r}}{N} \sum_{k=0}^{N-1} X(k) \Psi(s_r \omega_k) e^{i2\pi kn/N} \quad (3)$$

Next, we will graphically present this process in both time and frequency domains simultaneously and discuss the causes and consequences of edge effects and energy redundancy in the wavelet power spectra. The Morlet wavelet is chosen for the purpose of rotor-tip flow analysis, but the principle illustrated next applies to other continuous wavelet bases as well.

Graphical Derivation of Discrete Fourier Transform

The first step is to illustrate the process of taking the DFT. Although one can find such a graphical derivation of the DFT in many classical textbooks of digital signal processing, it is replicated in

Appendix A for completeness. For convenience, the following definition of the continuous Fourier transform is chosen:

$$H(f) = \int_{-\infty}^{\infty} h(t) e^{-i2\pi f t} dt$$

The inverse Fourier transform is thus

$$h(t) = \int_{-\infty}^{\infty} H(f) e^{i2\pi f t} df$$

For clarity, we choose a sinusoidal function to generate the time series so that the distortion in both time and frequency domains can be illustrated clearly. Referring to the table in Appendix A, the left column contains the time-domain terms and the right column contains the frequency-domain terms. Steps 1)–7) illustrate how the DFT and the inverse discrete Fourier transform (IDFT) are defined. Steps 8) and 9) generate the discrete frequency band that will be substituted into Eq. (3) for the DCWT.

One can see from steps 1)–7) in Appendix A that the DFT and the IDFT are defined in the intervals of $0 \leq f < f_1$ and $0 \leq \tau < T_0$, respectively, because of the window function that is used. Ideally, for a pure sinusoid we would expect an impulse in the frequency domain, but the DFT of the sinusoid is distorted because of the truncating window $w_1(\tau)$ introduced in step 4). Nevertheless, the finite-duration, discrete signal $x_2(\tau)$ [step 5)] can still be recovered as $x(n)$ by IDFT without distortion. In practice, when the FFT routines are applied, the number of data points N is required to be a power of 2 for the maximum computational efficiency. If necessary, $x_2(\tau)$ can be padded with zeros until its total length reaches the next power of 2. Padding $x_2(\tau)$ with zeros does not change the resulting DFT, $X_2(f)$, so that the remaining graphical steps 6) and 7) still hold, and $x(n)$ can be recovered through removal of the zeros after IDFT.

Sampling Wavelet Bases

In Appendix B, the process of sampling the frequency domain of wavelet bases is graphically demonstrated. First, regardless of what the scale s is, $\Psi(sf)$ has to be sampled at the same frequencies f as those for the DFT because Eq. (3) requires that $X(f)$ and $\Psi(sf)$ both be evaluated at the same frequencies before they can be multiplied together. This is why the same comb function that was used to sample the $X_2(f)$ [Step 6) in Appendix A] is also used here in Step 11) in Appendix B. However, because the sampling resolution in frequency is fixed for all scales the product $(s^* f)$ might be too coarse for large scales. This will cause aliasing in time domain [Step 12) in Appendix B]. Thus, aliasing poses an upper limit for the scale. Based on the experience with Nyquist's sampling theorem for time-domain signals, we state here, without mathematical proof, that to avoid aliasing in time domain the maximum scale must be such that the supports of the dilated wavelet bases in time domain must be less or equal to T_0 . The width of support for the Morlet wavelet can be considered to be $6s$ because this wavelet base function is indeed the Gaussian probability density function with standard deviation equal to s , and thus 99.97% of its energy is contained within a bandwidth of $\pm 3s$. So,

$$s_{\max} \leq \left(\frac{1}{6}\right) T_0$$

Otherwise, the aliased wavelet bases would create artifacts in the wavelet spectra.

After the wavelet base is sampled, the window function $W_2(f)$ has to be applied to truncate $\Psi(sf)$ [Step 13) in Appendix B], because it has to be the same length as $X_4(f)$ before it can be substituted into Eq. (3). Similar to the DFT, the window function will certainly cause distortion in time domain, which contributes to the edge distortion in the wavelet spectra. But unlike the DFT, truncating dilated wavelet bases can cause a new problem. It can cut off a part of $\Psi(sf)$ if the scale s is chosen too small. This imposes a lower limit in scales below which a part of high-frequency components can be cut off by $W_2(f)$. In other words, the minimum scale s_{\min} should be selected such that the support of $\Psi(s_{\min} f)$ is completely within the interval of

$0 \leq f < f_1$. Fortunately, s_{\min} is usually much less than the scale value corresponding to the sampling period T . Therefore, in practice, the minimum scale can be chosen as the value corresponding to the sampling period.

Once the DFT for the time series has been calculated and the wavelet bases are sampled, Eq. (3) can be applied, and the wavelet spectrum can be obtained. This is straightforward mathematically, yet difficult to show graphically, and so the graphical illustration will not be shown.

Edge Effect

At the edges where $\tau = kT_0$ and $k = 0, \pm 1, \pm 2, \dots$, a discontinuity can be generated if the total sampling time T_0 does not correspond exactly to the period of the original signal. This is caused by sampling in the frequency domain [(Steps 6) and 7), Appendix A], which replicates $x_2(\tau)$ every T_0 seconds in the time domain. This discontinuity will contribute to the so-called edge effect in wavelet spectra. If padding with zeros is necessary, one should be aware that it also creates a discontinuity at the edges of the original time series, and thus the edge effect.

The edge effect generated by discontinuities in the time series can be estimated by the cone of influence (COI). At any given scale s , an “e-folding” time t_m can be defined so that the spectral energy density of an impulse function drops by a factor of e^{-2} , as suggested by Ref. 14. For the Morlet wavelet, the COI can be shown to be $t_m = \sqrt{(2)s}$.

An additional contribution to the edge effect comes from the distortion at bounds that are created by the introduction of a window function in the frequency domain [$W_2(f)$ at Step 8) in Appendix A and Step 14) in Appendix B]. From the appendices, one can see that $W_2(f)$ causes a distortion in the time domain that alters the discrete signal. Nevertheless, the introduction of $W_2(f)$ is necessary because $X_3(f)$ and $\Psi(s_f)Y_1(f)$ cannot be directly used in the DCWT. The DFT and IDFT can be calculated without regard to the defined frequency range for $X_3(f)$, as long as the intervals are specified in which the definitions of the DFT and IDFT hold. Unfortunately, this is not the case for the DCWT. Only a band of $X_3(f)$ should be used in the DCWT and should be multiplied by the dilated discrete wavelet base. The rest of $X_3(f)$ should be cut off. $W_2(f)$ performs this cutoff, but it also generates distortions in the time domain.

The distortion generated by $W_2(f)$ also contributes to the edge effect of wavelet spectra. However, it is difficult to estimate this contribution. To minimize this distortion, an alternative window function can be used to replace $W_2(f)$. Because of the time constraint, this task remains as a challenge to be solved in the future.

Energy Redundancy

We now examine the effect of the nonorthogonality of the wavelet base. Consider s_1 and s_2 as two successive, discrete scales with $s_1 > s_2$. Because the wavelet base is not orthogonal, $\Psi(s_1 f)$ and $\Psi(s_2 f)$ are very likely to overlap each other (Fig. 2). If a signal $X(f)$ has a peak located in between s_1 and s_2 , the energy of $X(f)$ would spread into these two scale bands, and so it forms a large spot in the wavelet spectrum as if there were energy expanding from s_1 to s_2 . This is the so-called energy redundancy. If the wavelet bases were orthogonal, this energy-spreading phenomenon would not happen because $\Psi(s_1 f)$ and $\Psi(s_2 f)$ would not overlap.

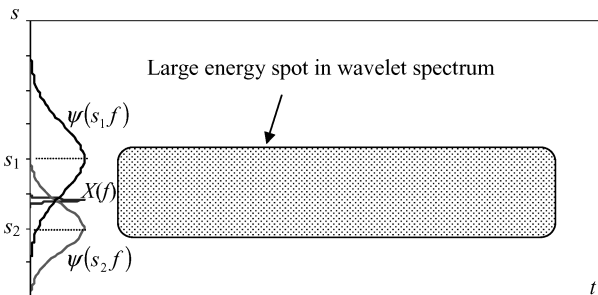


Fig. 2 Illustration of energy redundancy.

To reduce energy redundancy, it is necessary to set the intervals between any two successive scales as large as possible so that the spectra of wavelet bases do not overlap. However, this would then risk missing the peak of $X(f)$. Therefore, the intervals between discrete scales must be wisely chosen in order to compromise both scale resolution and energy redundancy reduction.

Consider the discrete scales distributed as the following:

$$s_j = s_0 a^j, \quad j = 0, 1, \dots, J$$

where s_0 is the scale value corresponding to the sampling period T . The value of s_J is equal to the allowable $s_{\max} (= T_0/6)$. To appropriately choose a and J , we note that the smallest resolution of discrete scales only needs to be as fine as the resolution of the discrete spectrum of the original time series, which is $1/T_0$. Hence, we have

$$\omega_0/s_{J-1} - \omega_0/s_J = 2\pi/T_0$$

and $s_J = s_0 a^J$. It follows that

$$a = 2\pi/6\omega_0 + 1, \quad J = \text{INT}[\ln(T_0/6s_0)/\ln(a)] \quad (4)$$

where INT rounds the value to its nearest integer towards zero.

Summary (Discrete Form of CWT)

1) The edge effect can be caused by discontinuities at the boundaries of the finite duration time series. It can be introduced when the continuous spectrum $X_2(f)$ is being sampled by $Y_1(f)$ [see Steps 6) and 7), Appendix A]. Padding with zeros also introduces this discontinuity. The influence range of these discontinuities can be estimated using an e-folding time t_m that defines the cone of influence. For Morlet wavelet, $t_m = \sqrt{(2)s}$.

2) The introduction of a window function in the frequency domain for the spectra of both the original time series and the wavelet base also contributes to the edge effect. Its influence is hard to estimate. However, it is anticipated that this kind of edge effect can be deduced with alternative window functions, which is a topic for future research.

3) The upper limit of the discrete scales must be wisely chosen so that aliasing in the time domain can be minimized. The lower limit is suggested to be the value corresponding to sampling period T . Finally, Eq. (4) is suggested as a means to determine the values of the discrete scales, while compromising the scale resolution and the reduction of the energy redundancy.

IV. Smoothing in Time and Scale

Torrence and Compo¹⁴ define a time-averaged wavelet spectrum as

$$\overline{WX}(s_r) = \frac{1}{n_2 - n_1 + 1} \sum_{n=n_1}^{n_2} WX_n(s_r)$$

where n_1 and n_2 are end points of the time segment to be averaged. This is also called the global wavelet spectrum (GWS). By repeating this operation for each time step, one creates a wavelet spectrum smoothed by a window. When applied to rotor-tip flows, this smoothing can enhance the peaks in wavelet power in the large-scale region. This makes it possible to track the speed of rotating flow disturbances.

A weighted sum of the wavelet power spectrum over a scale band of s_1 to s_2 provides information about the power fluctuations over time within this scale band:

$$\overline{WX}_n = \frac{T \log_2 a}{C_\delta} \sum_{j=j_1}^{j_2} \left[\frac{WX_n(s_j)}{s_j} \right]$$

where $C_\delta = 0.776$ for Morlet wavelet with $\omega_0 = 6$. As stated by Torrence and Compo,¹⁴ the scale-averaged wavelet power can be used to examine frequency modulation within the time series.

V. Characteristics of Rotating Disturbances

Consider a signal obtained from a pressure sensor located on the casing wall near the rotor-blade tips. In an ideal scenario, the compressor could be considered free from rotating spiky disturbances. So, one should see a “sawtooth” similar to the one shown in Fig. 3. Imagine a spike generated inside one or a few blade passages rotating at a speed different from the rotor speed. The sawtooth would then first be interrupted, and the sensor would pick up this spike at the interrupted location once every spike rotation. This is equivalent to saying that the higher frequency (carrier frequency) sawtooth is modulated with a binary on/off signal synchronized with the traveling speed of the spike (modulating frequency). The spike is then added onto the modulated signal. It can be shown mathematically that although such a modulation produces many frequency components on the Fourier and wavelet spectra there will be two groups of frequencies (or scales) each with a fundamental frequency. One of the fundamental frequencies will be centered at the carrier (blade passage) frequency, and the other will be centered at the modulating (spike) frequency. To illustrate this argument, consider an artificial signal that is created through a modulation described as

$$f(t) = x(t)*y(t) + u(t)$$

where $x(t) = 1.0 \sin(\omega t)$ is the signal at the carrier frequency and the binary on/off signal is produced with a traveling square wave ($y=0$ between θ_0 and $\theta_0 + \Delta\theta$; $y=1$ otherwise) as sensed by a

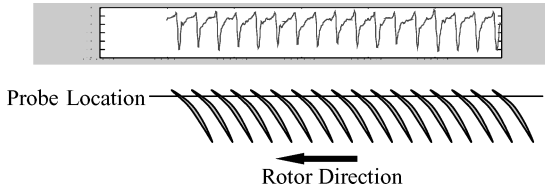


Fig. 3 Sawtooth signal from a sensor located on top of rotor case.

probe located at θ_1 :

$$y(t) = \begin{cases} 0 & \text{if } \theta_1 - \theta_0 - \Delta\theta \leq ct \leq \theta_1 - \theta_0 \\ 1 & \text{otherwise} \end{cases}$$

where c is the traveling speed of the spike. The spike $u(t)$ is defined as follows:

$$u(t) = \begin{cases} 0.6 & \text{if } y = 0 \\ 0.0 & \text{otherwise} \end{cases}$$

Figure 4a depicts $f(t)$ in the time domain, while Figs. 4b–4d show its wavelet spectrogram, global wavelet spectrum, and Fourier power spectrum, respectively. The horizontal axes in Figs. 4a and 4b are time in the unit of seconds. The cone of influence is marked in Fig. 4b with two solid curves that join in the middle and form a bowl-shape line, below which the edge effects are significant. In the figure, $\omega = 64\pi$, $c = 2\pi$ and $\Delta\theta = 22.5$ deg. From Fig. 4d, one can clearly identify the two fundamental frequency groups, one of which is centered at a frequency of 32 Hz and the other at 1 Hz. The group at 32 Hz corresponds to a blade passing frequency, and the group at 1 Hz corresponds to the spike passing frequency. Other spectrum components are simply the byproducts of the modulation. Correspondingly, in Figs. 4b and 4c peaks can be identified at two 32 and 1 Hz (horizontal lines). However, the wavelet spectrogram does one thing more than the Fourier spectrum: it identifies the location and size of the spike. Between the frequency ranges from 32 to 1 Hz, there are isolated spots showing the location and size where energy is localized. These spots coincide with the spike very well.

In summary, when spikes occur in the blade passages, the following characteristics appear in the wavelet spectrogram:

- 1) The blade passage sawtooth pattern is broken by amplitude modulation, allowing the spike to appear in the signal.
- 2) The spike generates many components in the WT spectrogram, ranging from short scale (high frequency) to long scale (low frequency). These components are all related to the same spike so they cannot be treated as independent disturbances.
- 3) The energy of spike is localized on the wavelet spectrogram so that one can identify its time and size.

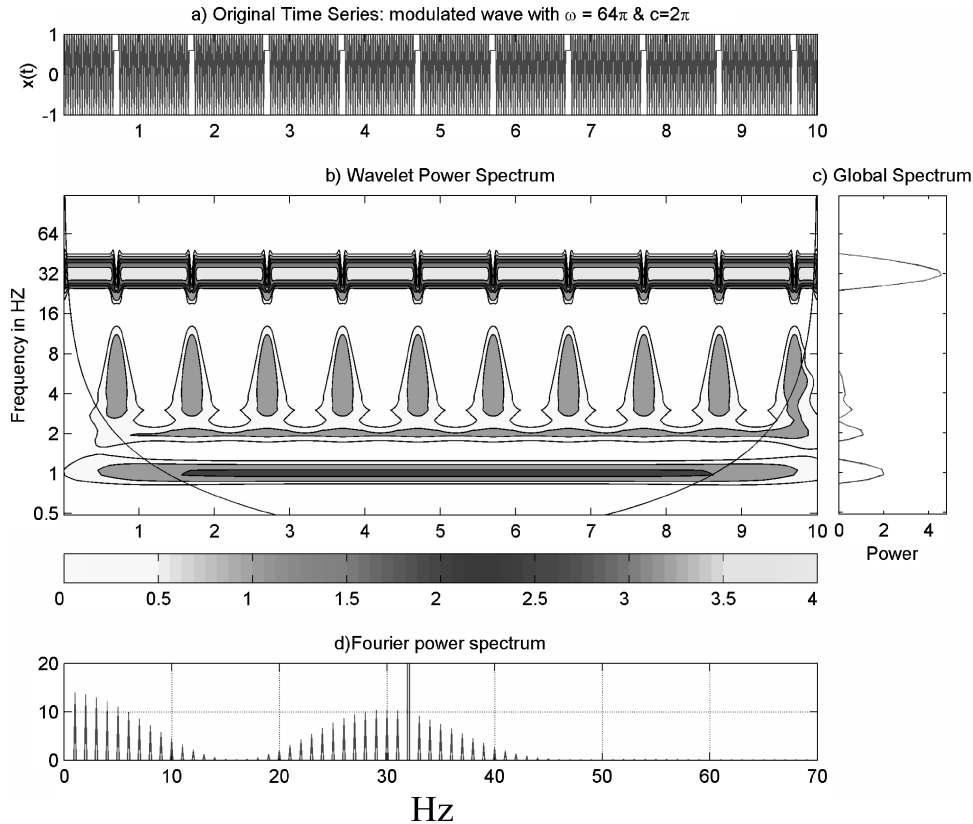


Fig. 4 Characteristics of rotating disturbances. The horizontal axis for Fig. 4d is frequency given in hertz.

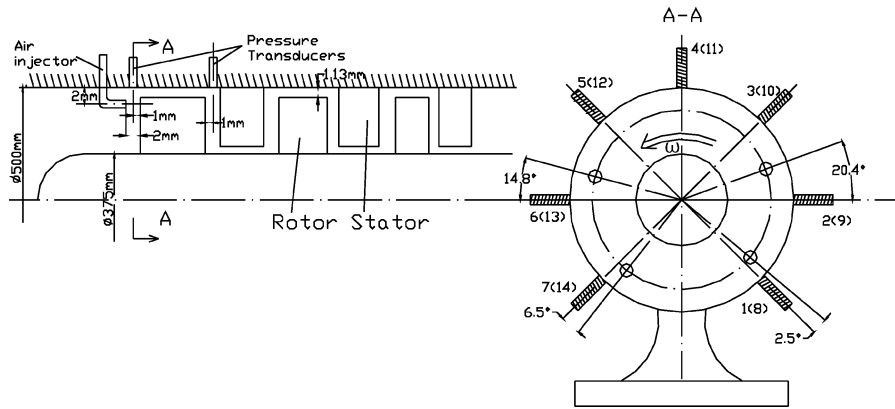


Fig. 5 Schematic illustration of the test facility and sensor locations.

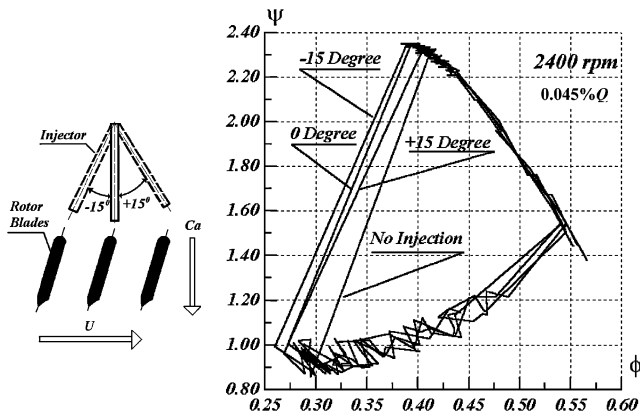


Fig. 6 Steady compressor performance with and without micro air injection.

VI. Test Facility

The test facility is described in detail in Nie et al.,¹⁶ where the benefit and the unsteady effect of micro air injection in the tip region of the first rotor were investigated. Figure 5 depicts schematically the experimental configuration, including the location of the sensors. The test compressor is a three-stage low-speed axial compressor with a design speed of 2400 rpm. There are 58 blades for each rotor and stator. The overall compressor performance in terms of total-to-static pressure rise coefficient ($\Psi = \Delta p / 0.5 \rho U^2$), and flow coefficient ($\Phi = V_x / U$) is measured with eight static pressure taps on casing and around the annulus in both inlet and outlet of the compressor. Seven, high-response, Kulite transducers (sensors 1–7) are located around the annulus on the casing in front of the first rotor. Another seven transducers (sensors 8–14) are located behind the first rotor. These sensors are spaced 45 deg apart between each sensor pair and 90 deg apart between sensor 1 and 7 (also 8 and 14) because of the rig support stand located between sensors 1 and 7 (Fig. 5). The sampling rate is 16 kHz. The Kulite XCS190 transducers all have a rated pressure of 34.475 kPa (5 psi) and a sensitivity of 3.75 mV/kPa. The transducer's zero pressure output is less than $\pm 5\%$ of full scale.

Figure 6 gives the compressor performance with and without microinjection. The definition of injection angle is also given in the figure. Nie et al.¹⁶ demonstrated that, even though the injected mass flow rate was as low as 0.045% of the compressor flow rate, the mass flow at stall was decreased by 5.83% and the pressure coefficient at stall was increased by 1.12% (for the injection angle of -15 deg as indicated in Fig. 6).

Throughout this paper, we will use the voltage values as sampled by the computer data-acquisition system to represent the pressure signal. Also, the test data do not include the instantaneous throttle position corresponding to the instantaneous compressor operating point. This information would be useful to further unearth the triggering mechanism of the captured disturbances. This does not cause

a problem with the current research as the main purpose is to demonstrate the signal processing tool.

VII. Results

Fourier-Based Low-Pass Filtering Result

Figure 7 displays the raw pressure signal from sensor 1 and its low-pass filtered result. The cutoff frequency is set to be twice the rotor frequency. This is similar to what Garnier et al.¹ did, when they provided evidence for the existence of modal waves. Apparently, no modal activity can be found by visual inspection of the low-pass filtered data for this test compressor. The stall is triggered by a spike that occurs immediately prior to stall.

Some researchers filtered the raw data before taking the wavelet transform. Caution should be taken if filtering is performed because an improper cutoff frequency will smear the true spike and thus defeat the purpose of wavelet analysis. It is hard to determine the proper cutoff frequency prior to analysis. Also, because the wavelet transform is a bank of bandpass filters there is no need to do Fourier-based filtering before the wavelet analysis. For this reason, the wavelet analyses in this paper are all done on the raw data.

Structural Asymmetry and Rotor Vibration

In Fig. 8, the wavelet transform is applied to the data of pressure sensor 1. The horizontal axis for Figs. 8a and 8b is time in the unit of rotor revolution prior to stall onset. The same is true for all of the rest of the figures in this paper. Because this is the early prestall period, we expect the compressor to be free from rotating disturbances. The wavelet spectrogram (Fig. 8b) shows this is indeed the case. There are three energy bands in this spectrogram. One is centered on $58 f_{\text{rot}}$, one on $1 f_{\text{rot}}$, and the third one between $8 f_{\text{rot}}$ and $32 f_{\text{rot}}$. The isolated spots between $8 f_{\text{rot}}$ and $32 f_{\text{rot}}$ are periodic with a period of 1 rotor revolution (rev.), which indicates that there is a structural asymmetry in the first rotor row of this compressor. The energy bands in $58 f_{\text{rot}}$ (the blade passage frequency) and $1 f_{\text{rot}}$ appear across the entire time sample.

To identify whether or not the structural asymmetry ($8-32 f_{\text{rot}}$) is rotating relative to the stationary coordinate frame, other sensors are also examined. Figure 9 depicts the wavelet spectra between $16 f_{\text{rot}}$ and $32 f_{\text{rot}}$ for all seven sensors. Even though the signal might be weak at any particular point, it is still recognizable that this structural asymmetry propagates around the annulus at a speed equal to the rotor speed. A diagonal line is drawn across all sensor traces in Fig. 9 to show this propagation. This means that the structural asymmetry is located on the rotor, which sweeps through each sensor as it rotates with the rotor. For this reason, we call it a rotating asymmetry.

Size and Location of the Spike When Initiated

Wavelet analysis can help to identify the size and location of spiky disturbances, unlike other signal processing methods. After processing the first 10 rotor revolutions of data as shown in Figs. 8 and 9, the same processing is done on subsequent time segments of data for all seven sensors. Similar wavelet spectra are produced,

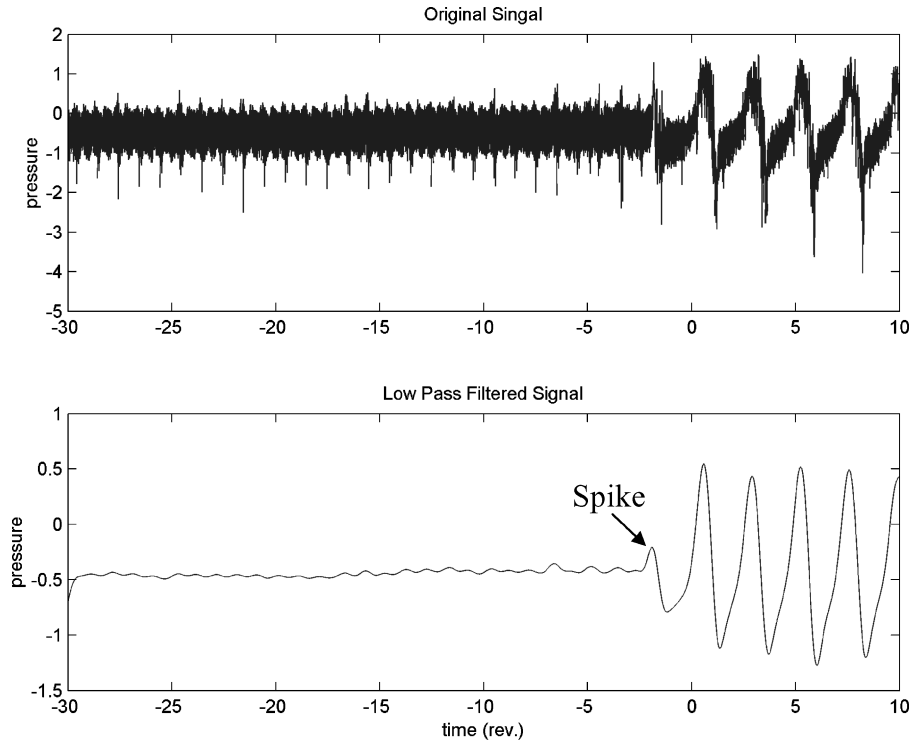


Fig. 7 Original and filtered signal from sensor 1 without injection.

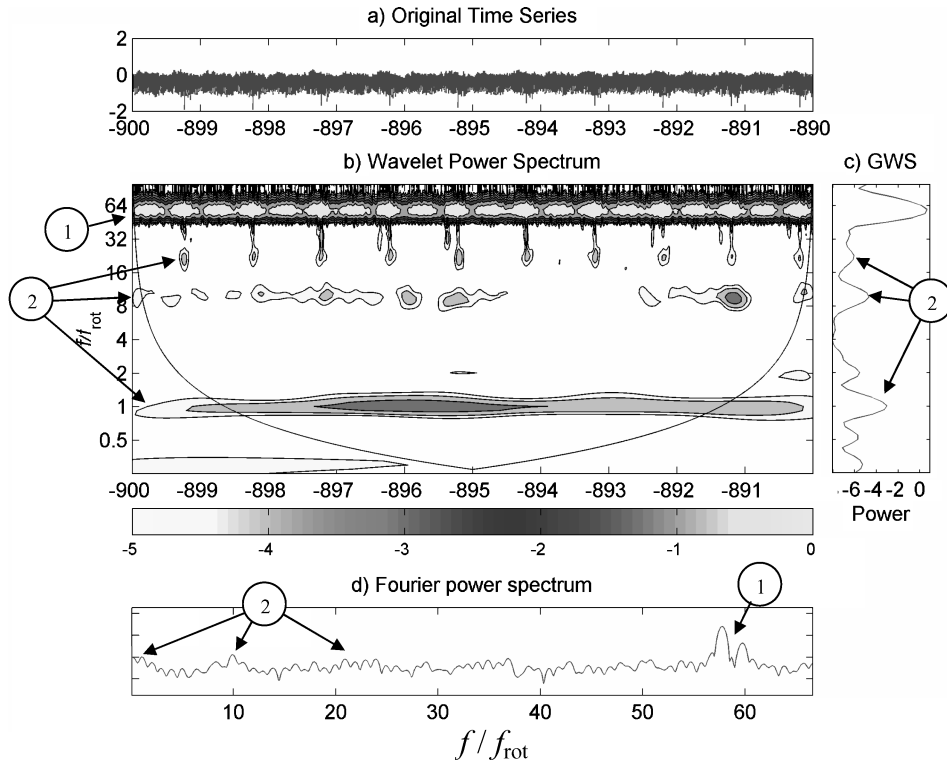


Fig. 8 Wavelet spectrogram and the Fourier spectrum for a data segment from sensor 1.

as shown in Fig. 10 for sensor 1 and in Fig. 11 for all sensors. In Fig. 10, three spikes can clearly be seen in the band between $4f_{\text{rot}}$ and $32f_{\text{rot}}$ in the 10 revolutions between -446 and -456 . They are located on or near the rotating asymmetry. This is not a coincidence because spikes are initiated on or near the rotating asymmetry in all of the tests performed on this compressor. The size of the spikes can be identified in Fig. 10. Close inspection shows a spike being initiated at about rotor revolution -452.4 (Spike ii as marked in

Fig. 11), which can be seen clearly in the raw data (Fig. 10a). The spike spreads energy over a wide range of frequencies/scales and generates a spectrum of discontinuity in the time domain. Because of the edge effects discussed in Sec. III and illustrated in Fig. 4 with an artificial signal, the isolated spot between $4f_{\text{rot}}$ and $32f_{\text{rot}}$ can occupy as large as half of the rotor revolutions in horizontal time axis. This spread is simply the component of the wavelet spectra generated by the short-length-scale spike and does not mean the size

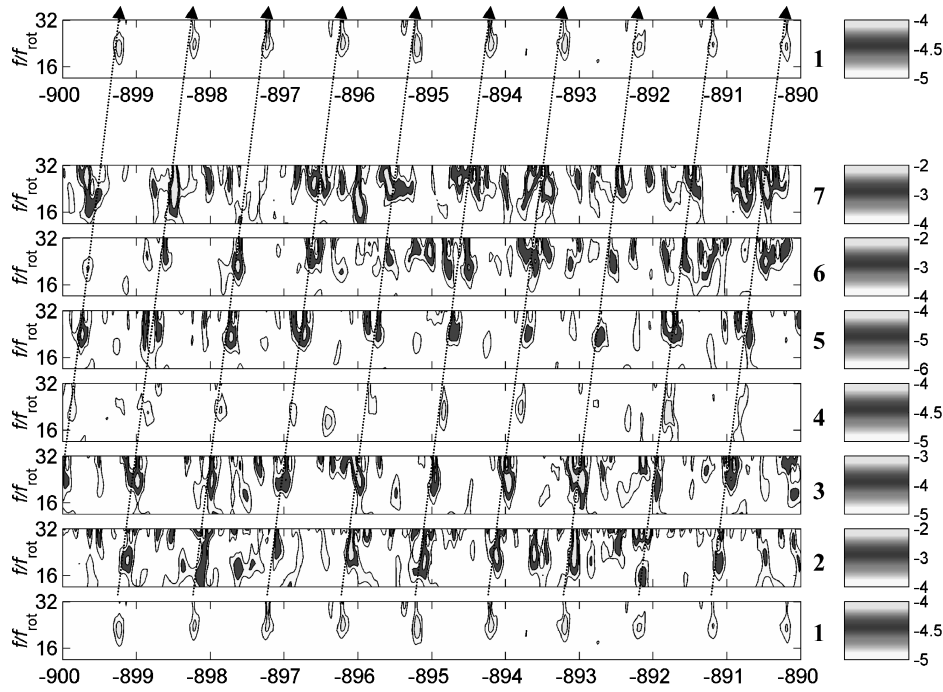


Fig. 9 Parallel wavelet spectra for the period of -900 to -890 revolutions.

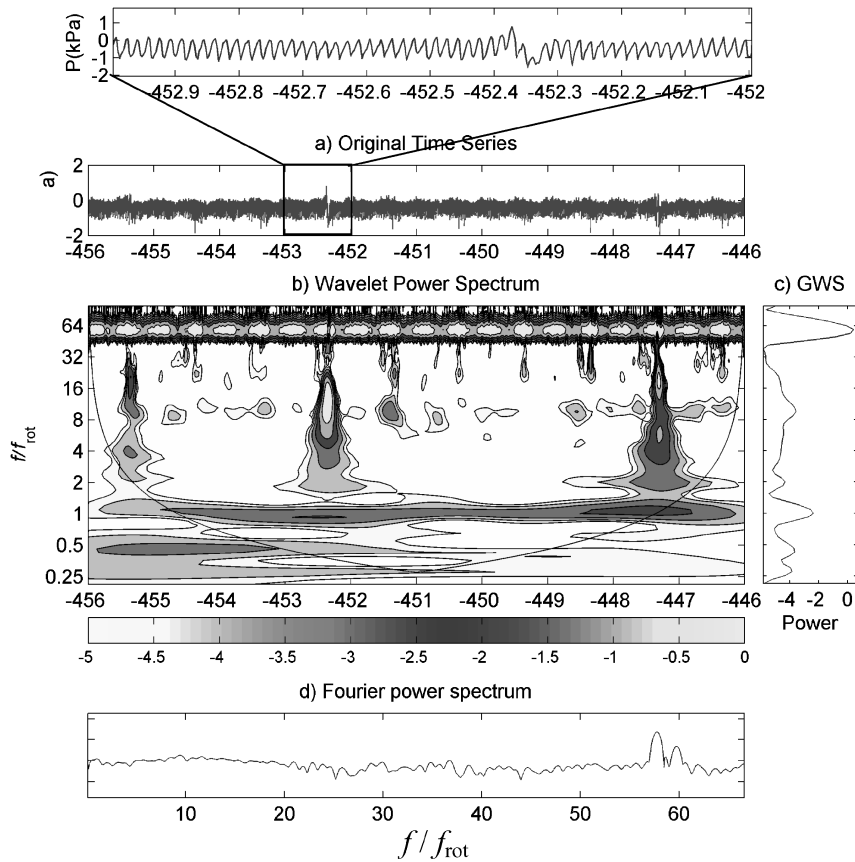


Fig. 10 Wavelet spectrum for sensor 1 at -456 revolutions before stall.

of the spike was as large as half of the rotor annulus. In fact, from the inspection of the raw data in this region we were able to identify that this spike occupied about four blade passages (Fig. 10a) out of the 58 blades on this rotor. This is obviously not modal activity.

In Fig. 11, the bands of $4f_{rot}$ and $32f_{rot}$ in the wavelet spectra for all seven sensors are placed in parallel for the same data segment. Sensor 1 is repeated on the top to illustrate the cyclic placement of sensors. Although it is very weak compared to the spikes, the

rotating asymmetry is still recognizable. By comparing the trace of the spikes with that of rotating asymmetry, we can clearly see that the spikes travel at about 60% of the rotor speed. The spike is probably initiated in the vicinity of sensors 1 and 7 or somewhere between them. This latter observation gives us a hint that there is another unknown mechanism that is fixed in the vicinity of sensors 1 and 7 or between them, which triggers spikes when interacting with the rotating asymmetry. We will call this unknown mechanism

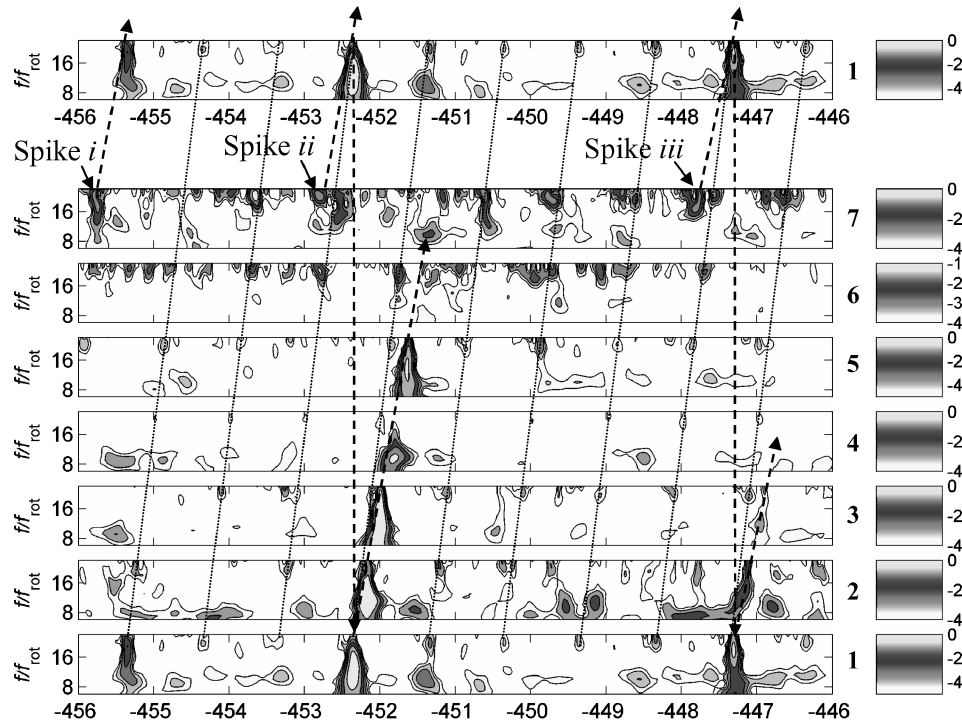


Fig. 11 Parallel wavelet spectra for the period of -456 to -446 revolutions.

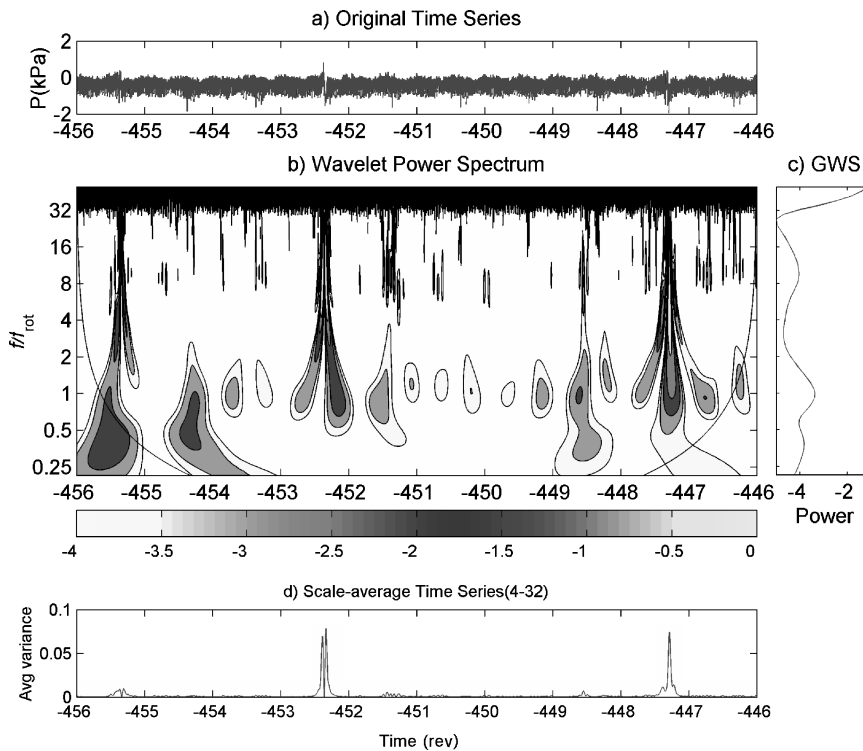


Fig. 12 Wavelet spectrum of the same data segment as Fig. 10 using Mexican hat wavelet.

a stationary asymmetry to contrast it with the rotating asymmetry. At this point, it is not clear to us what caused the asymmetries, but we do know that their interaction triggers spikes.

To illustrate the importance of the choice of wavelet base, we use the Mexican hat wavelet to transform the same data and generate Fig. 12. One can see that the Mexican hat wavelet can clearly track the instants of spike appearances because of its excellent resolution in time domain, but its poor frequency resolution degrades the modulation between the blade passage frequency ($58f_{rot}$) and the rotor rotating frequency ($1f_{rot}$).

Intermittent Pattern of Spike Evolution

Spikes like the ones depicted in Figs. 10 and 11 come and go. They form an intermittent pattern of spike evolution. In Fig. 11, it is clear that all three spikes rotate from one sensor to another at about 60% of the rotor speed. All of them disappear before they return to where they were initiated. What is more interesting to us is that as the compressor is throttled closer to the stall boundary and the spikes appear more frequently and last longer. Figures 13 and 14 give a typical example to demonstrate this point. Four spikes are initiated within this 10 revolutions of time. Spike 1 in Fig. 14 lasts

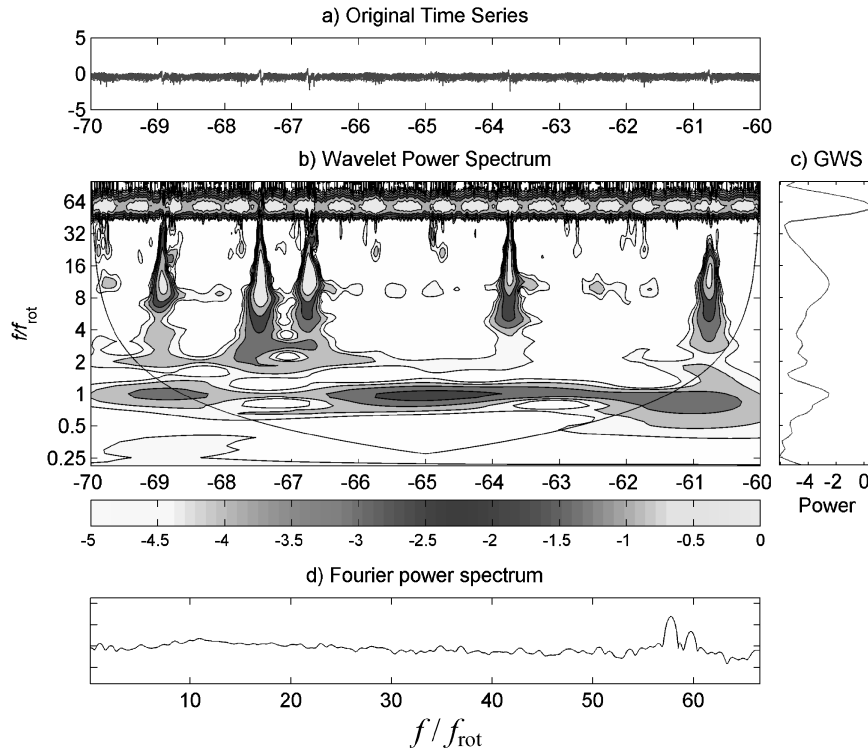


Fig. 13 Wavelet spectrum for sensor 1 at -70 revolutions before stall.

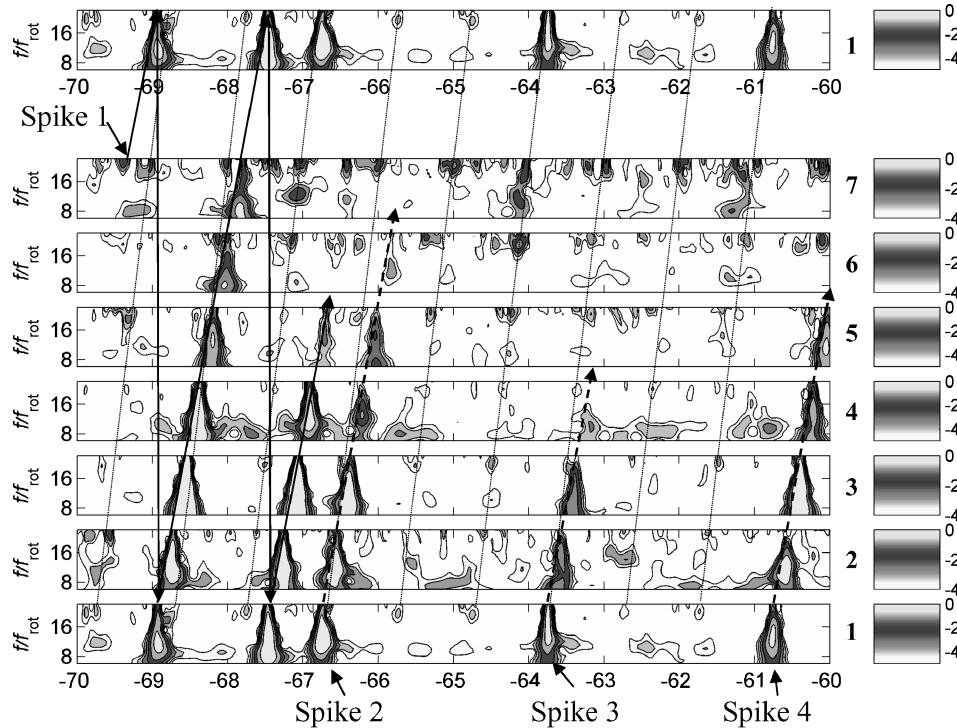


Fig. 14 Parallel wavelet spectra for the period of -70 to -60 revolutions.

more than one revolution. Taking a close look of the propagation process of Spike 1, one can notice that its strength decays slightly as it travels from sensor 1 to sensor 7 but is reinforced once it encounters sensor 1 again. It seems related to the same stationary asymmetry as described for Fig. 11.

Figure 15 depicts how the stall is finally triggered. Among the four spikes initiated in this period, only one of them (Spike c) finally develops into full stall. Spike c goes through an initiation-weaken-strengthen process and finally triggers the system instability.

The entire process can be summarized using the GWS. As shown in Fig. 16, the band between $4f_{\text{rot}}$ and $32f_{\text{rot}}$ depicts the intermittent pattern of spiky disturbances in the entire throttling-to-stall process. One can see that in this particular test the spiky activity is not very active until about -200 rotor revolutions.

Prestall Process with Microinjection

The same analysis is applied to prestall processes with micro air injection. Figure 17 depicts a comparison among the three

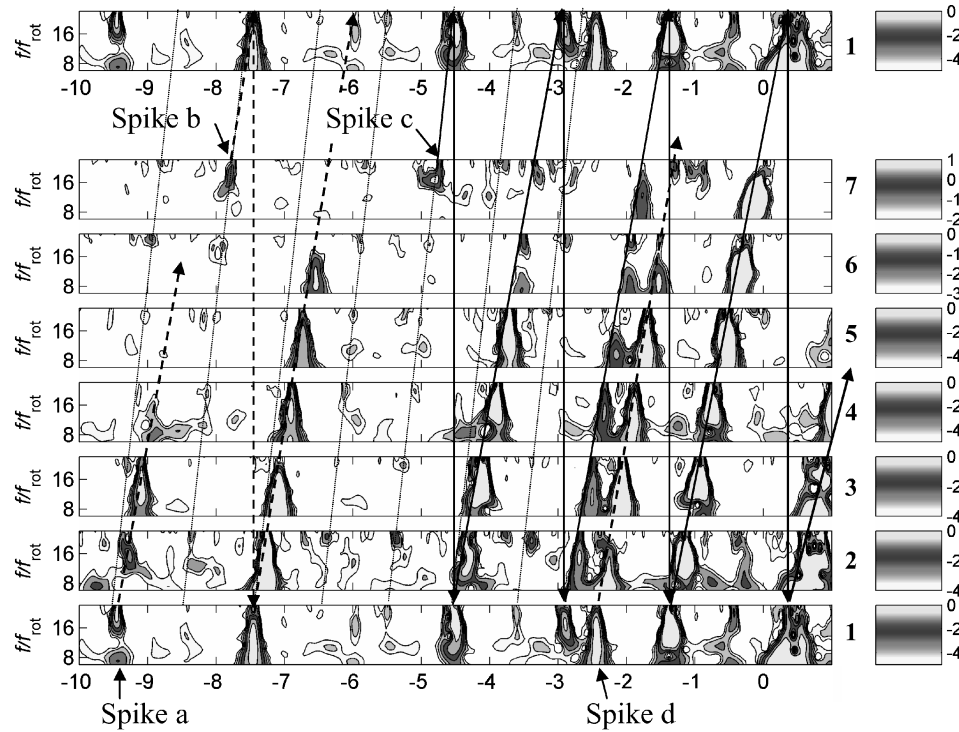


Fig. 15 Among the four spikes born within 10 revolutions before stall, only Spike c grew into full stall.

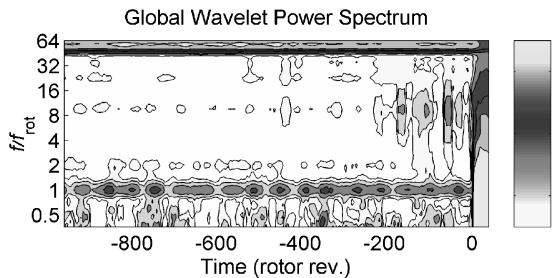


Fig. 16 GWS of the signal from sensor 1 without air injection.

microinjection tests with -15° , 0° , and 15° injection angles, respectively. The band of interest is the band between $4f_{rot}$ to $32f_{rot}$, and so the comparison is made only for this band. This comparison shows that the compressor was more stable when the micro air injection reduced the frequency of the appearance of the spiky disturbances.

VIII. Discussions

Although the wavelet transform is a powerful signal processing tool, typically it is difficult for wavelet users to relate the results of the wavelet transform to the signal physics. One of the main reasons for this difficulty is that, unlike the classical Fourier transform, a wavelet transform has many options. An inappropriate configuration choice can lead to meaningless or misleading results. The first half of this paper filled the gap between theory and practice by resolving several practical issues of the wavelet transform within the context of rotor tip flow analysis. The authors studied the process of implementing one-dimensional continuous wavelet transforms discretely on computers with a graphical derivation process. The graphical derivation becomes the vehicle to identify the causes and to estimate the consequences of edge effect and energy redundancy. The minimum and maximum scales are also determined. Although this paper is targeted to the application of rotor-tip disturbances, these results are general enough to help researchers to configure the wavelet tool so that it will be better suited for any applications that researchers might have.

With the help of the well-configured wavelet tool developed in the first half of the paper, the second half reports the discovery of the intermittent pattern of spiky disturbances in a three-stage low-speed axial compressor. In the early period of the prestall process, the compressor was free from spikes, but the sensors did pick up a rotating asymmetry. As the compressor was throttled towards the stall limit, spiky disturbances were initiated but immediately suppressed by the compressor. The closer the throttle is to the stall limit, the more frequent the spiky disturbances appear. With the sizes generally less than four blade passages, these spikes are initiated when the rotating asymmetry moves through the vicinity between sensors 1 and 7. This hints that there is a fixed asymmetry in this region. These spikes come and go. Only a spike initiated within 10 revolutions prior to stall eventually grew into full stall. This research finding can open a door to solve the mystery of spiky stall inception, because for the first time a spiky disturbance in the early stage of the prestall process is clearly tracked both in the time and space. Although the spike was initiated abruptly and grew into full stall within a very short period of time, the wavelet analysis shows that the spiky inception has a long evolution.

It is of importance to note several measurement issues that might likely be ignored by compressor experimenters targeting flow physics of stall development, which are locations of sensors, sensor calibration, signal preconditioning, and an appropriate sampling rate. First, when the stall is triggered by the flow disturbances within the rotor-blade tips it is crucial to have the sensors pick up the sawtooth pattern generated by rotor blades. If a sensor is located in the inlet that is far away from the first rotor, the pressure fluctuation caused by spiky disturbances in their early stage might be too weak to propagate to the sensor and thus might not be detected. Hence, the sensors must be located close enough to the first rotor or wherever the spikes are expected to appear. Second, in order to track the disturbances from one sensor to another all of the sensors around the annulus should be calibrated so that they have identical sensitivity to the flow disturbances. Third, caution must be taken in regards to signal preconditioning. Common signal preconditioning includes prefiltering the signal with an analog filter before it reaches the data-acquisition board, low-pass filtering the collected data, and resampling the data at a lower sampling rate. All of these popular practices can destroy the ability to track the spiky disturbances and

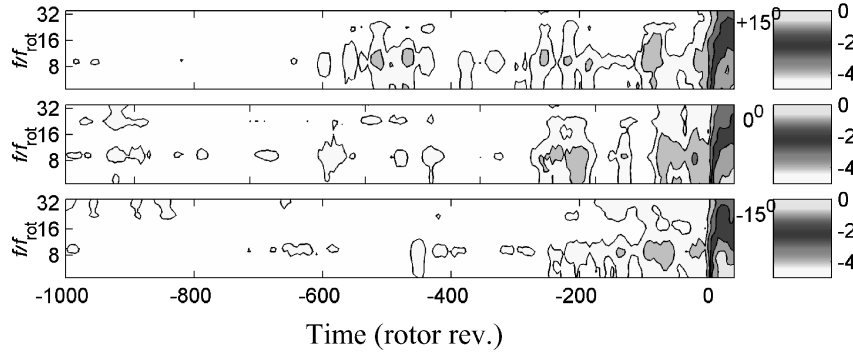


Fig. 17 GWS comparison for the micro air injection tests with various injection angles.

therefore should be avoided. (An antialiasing filter with a cutoff frequency set at just under the Nyquist frequency is still recommended.) Finally, choosing an appropriate sampling rate is very important to preserve the ability to track the spikes. Because the spike signals are embedded in the blade passage flows, it is necessary to have the sampling rate high enough to cover the flow variation within the blade passage. For example, for the tested compressor in this research, one might intuitively think that a sampling rate of 500 Hz is high enough for the low-speed compressor running at 40 Hz (2400 rpm). However, in order to have at least five samples within each blade passage we need to have a sampling rate of at least 11,600 Hz ($= 5 \text{ samples/blade} \times 58 \text{ blade/rev} \times 40 \text{ rev/s}$). We actually chose 16,000 Hz in this paper. In the past, many experimenters avoided such a high sampling rate because the enormous volume of data it might have produced. Unfortunately reduction of data volume can also lose useful information. Care must be taken in this regard.

Because the test compressor's instability was not triggered by modal waves, it is hard at this point to justify the effectiveness of the current wavelet tool to modal waves. Nevertheless, the authors are confident that the wavelet analysis is well suited to detect modal waves because the fundamentals of the blade passage flow physics and the signal analysis remain the same.

IX. Conclusions

The following conclusions can be made with regard to practical aspects of wavelet analysis:

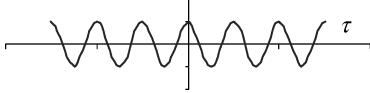
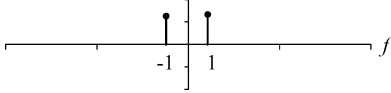
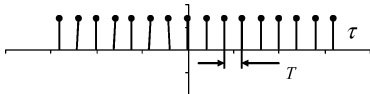
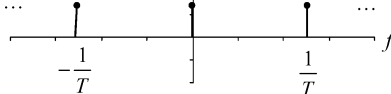
1) Guidelines are given for choosing a wavelet base for a specific application. In particular, for the rotor-tip flows the choice of the wavelet base is a compromise between the resolution requirements in both frequency and time.

2) The edge effects can be caused by both introducing discontinuity into the time series and applying a window function to cut out the frequency bands for both the original signal and the wavelet base. The range of influence, caused by the discontinuities, can be estimated using an e-folding time that defines the cone of influence.

3) The upper limit of the discrete scales must be chosen wisely to minimize aliasing in the time domain. We suggest a lower limit equal to the sampling period. A scheme to determine the set of discrete scales is also suggested in order to minimize the effect of energy redundancy.

This research demonstrates that with properly collected data and with the proper use of the wavelet it is now possible to uncover many details of the behavior of the spiky prestall disturbances and that their size, place, and time of initiation and evolution can be tracked. Two kinds of asymmetries, rotating and stationary asymmetries, are identified. Their interaction triggers the spikes throughout the entire prestall period. In future studies, the same wavelet analysis approach can be used to investigate other mechanisms that can contribute to compressor instability, such as the transient behavior of throttle closing and the variation of blade loading. The study of throttle closing helps to understand the intermittent pattern of spike evolution, whereas the study of the variation of blade loading helps to understand the role of modal and spike precursors and perhaps their interrelation in triggering compressor instability.

Appendix A: Graphical Derivation of DFT

Step	Time domain, $h(t) = \int_{-\infty}^{\infty} H(f)e^{i2\pi ft} df$	Frequency domain, $H(f) = \int_{-\infty}^{\infty} h(t)e^{-i2\pi ft} dt$
1)	 <p>Given a signal to be sampled $x(\tau) = \cos(2\pi\tau)$, $-\infty < \tau < \infty$, sampling it digitally with a sampling period T for a finite duration of $[0, T_0]$, is equivalent to having it first multiplied by a sampling function and then by a window function $w_1(\tau)$ in time domain.</p>	 <p>The Fourier transform (FT) of $x(\tau)$ is</p> $X(f) = 1/2[\delta(f - 1) + \delta(f + 1)]$
2)	 <p>The sampling function is a comb function:</p> $y_0(\tau) = \sum_{n=-\infty}^{\infty} \delta(\tau - nT)$ <p>where T is the sampling rate.</p>	 <p>The FT of $y_0(\tau)$ is also a comb function:</p> $Y_0(f) = 1/T \sum_{n=-\infty}^{\infty} \delta\left(f - \frac{n}{T}\right)$

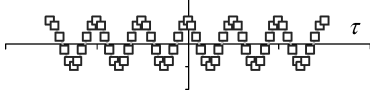
(Continued)

(Continued)

Step Time domain, $h(t) = \int_{-\infty}^{\infty} H(f) e^{i2\pi ft} df$

Frequency domain, $H(f) = \int_{-\infty}^{\infty} h(t) e^{-i2\pi ft} dt$

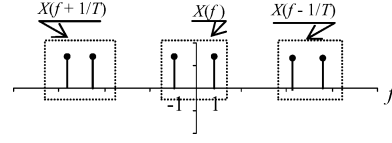
3)



$x_1(\tau) = x(\tau)y(\tau)$ produces an infinitely long, discrete time series:

$$x_1(\tau) = \sum_{n=-\infty}^{\infty} x(nT) \delta(\tau - nT)$$

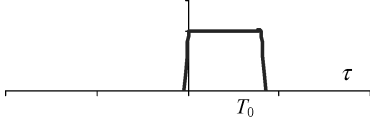
A window function is introduced next to truncate this time series.



$$X_1(f) = X(f) * Y_0(f) = 1/T \sum_{n=-\infty}^{\infty} X(f - n/T)$$

where * represents convolution. Note that if $1/T$ were less than the Nyquist frequency ($=2$ in this special example), $X(f - n/T)$ would be overlapping with its neighbors, which causes alias in time domain.

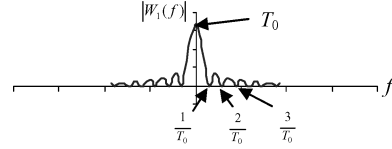
4)



The window function that is used to truncate $x_1(\tau)$ is

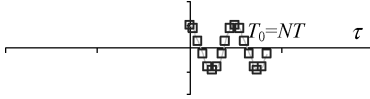
$$w_1(\tau) = \begin{cases} 1 & -\varepsilon < \tau < T_0 - \varepsilon \\ 0 & \text{otherwise} \end{cases}$$

where ε is a small positive number.



$$W_1(f) = \frac{\sin(\pi f T_0)}{\pi f} e^{-i2\pi f T_0}$$

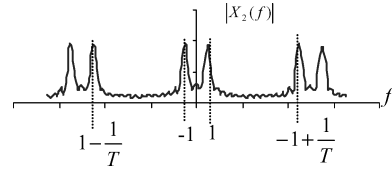
5)



The discrete time series with finite duration is

$$x_2(\tau) = x_1(\tau)w_1(\tau) = \sum_{n=0}^{N-1} x(nT) \delta(\tau - nT)$$

Note that the introduction of $W_1(\tau)$ causes a distortion in the frequency domain. Increasing T_0 will reduce this distortion.

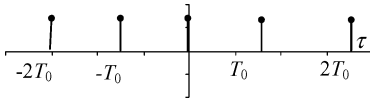


The FT can be derived using $X_1(f) * W_1(f)$, but it is easier to obtain following by directly taking FT of $x_2(\tau)$:

$$X_2(f) = \sum_{n=0}^{N-1} x(nT) e^{-i2\pi f nT}$$

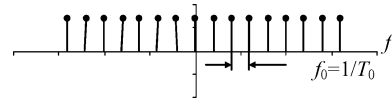
Note that $X_2(f)$ is a periodic function with period $1/T$.

6)



The inverse FT of the comb function $Y_1(f)$ is

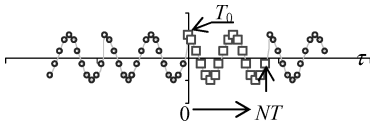
$$y_1(\tau) = T_0 \sum_{k=-\infty}^{\infty} \delta(\tau - kT_0)$$



Because $X_2(f)$ is still continuous, a comb function is used to sample it:

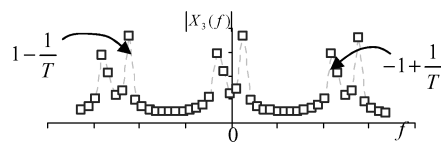
$$Y_1(f) = \sum_{k=-\infty}^{\infty} \delta(f - kf_0)$$

7)^a



The inverse FT of $X_3(f)$ is

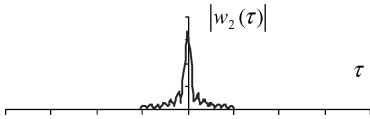
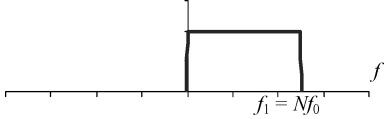
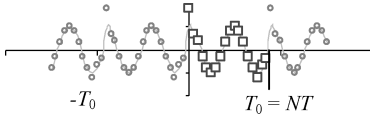
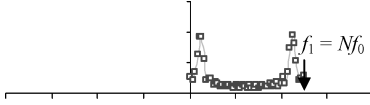
$$x_3(\tau) = x_2(\tau) * y_1(\tau) = T_0 \sum_{k=-\infty}^{\infty} \sum_{n=0}^{N-1} x(nT) \delta(\tau - nT - kT_0)$$



The discrete frequency domain is

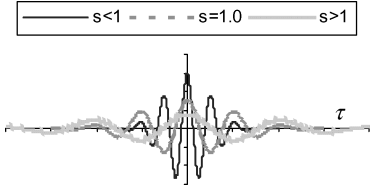
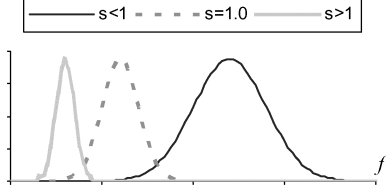
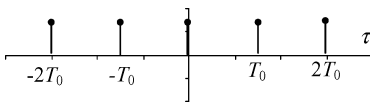
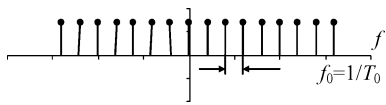
$$X_3(f) = X_2(f)Y_1(f) = \sum_{k=-\infty}^{\infty} c_k \delta(f - kf_0)$$

(Continued)

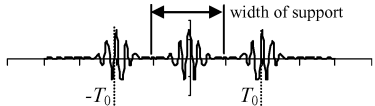
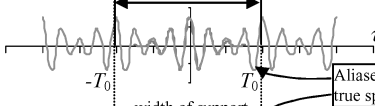
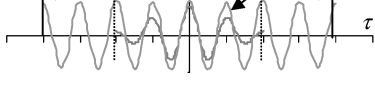
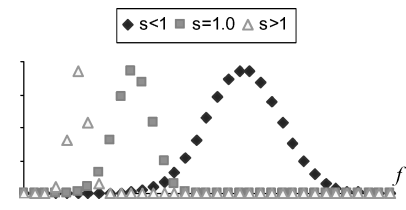
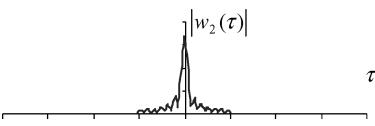
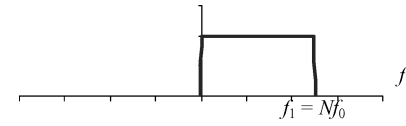
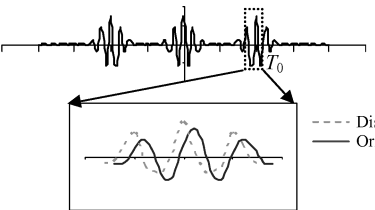
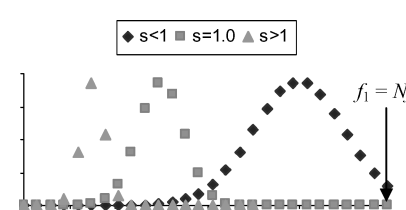
Step	Time domain	Frequency domain
	<p>Time domain, $h(t) = \int_{-\infty}^{\infty} H(f) e^{i2\pi ft} df$</p> <p>It is a periodic function with period T_0, so that it can be expanded as a Fourier series: $x_3(\tau) = \sum_{k=-\infty}^{\infty} c_k e^{i2\pi f_0 k \tau}$, and</p> $c_k = \frac{1}{T_0} \int_{-\varepsilon}^{T_0+\varepsilon} x_3(\tau) e^{-i2\pi f_0 k \tau} d\tau = \sum_{n=0}^{N-1} x(nT) e^{-i2\pi kn/N}.$ <p>Because $x_3(\tau)/T_0$ in the interval $0 \leq \tau < T_0$ is indeed $x_2(\tau)$, we thus have the IDFT as</p> $x(n) = 1/N \sum_{k=0}^{N-1} X(k) e^{i2\pi kn/N}$	<p>Frequency domain, $H(f) = \int_{-\infty}^{\infty} h(t) e^{-i2\pi ft} dt$</p> <p>where $c_k = \sum_{n=0}^{N-1} x(nT) e^{-i2\pi kn/N}$. Note that this c_k is exactly the same as the Fourier coefficient of $x_3(\tau)$. We now obtain the DFT of $x(n)$ as follows</p> $X(k) \equiv \sum_{n=0}^{N-1} x(n) e^{-i2\pi kn/N}$
8)	 $w_2(\tau) = \frac{\sin(\pi f_1 \tau)}{\pi f_1 \tau} e^{i2\pi f_1 \tau}$ <p>where $f_1 = Nf_0$.</p>	 <p>The window function that truncates the discrete frequencies is</p> $W_2(f) = \begin{cases} 1 & -\varepsilon < f < f_1 \\ 0 & \text{otherwise} \end{cases}$
9)	 $x_4(\tau) = \sum_{k=0}^{N-1} c_k e^{i2\pi f_0 k \tau}$ <p>Note that the edges at kT_0 are distorted because of the convolution with $w_2(\tau)$.</p>	 <p>The discrete frequency band that will be applied to DCWT:</p> $X_4(f) = X_3(f) W_2(f) = \sum_{k=0}^{N-1} c_k \delta(f - kf_0)$

^aThe graphical derivation of DFT stops here at the end of this step. However, when applied to DCWT, the following two additional steps are necessary because only the band of $X_3(f)$ in $0 \leq f < f_0$ will be used in DCWT.

Appendix B: Sampling Frequency-Domain Wavelet Base

Step	Time domain	Frequency domain
10)	 $(1/s) \psi(\tau/s) = s^{-1} \pi^{-\frac{1}{4}} e^{i\omega_0 \tau/s} e^{-(\frac{1}{2})(\tau/s)^2}$ <p>Morlet wavelet is chosen as an example. Only the real part is plotted here.</p>	 $\Psi(sf) = \pi^{-\frac{1}{4}} H(f) e^{-(2\pi sf - \omega_0)^2/2}$ <p>Note that large s corresponds to narrow supports in frequency domain and large supports in time domain.</p>
11)	 <p>The inverse FT of the comb function $Y_1(f)$ is</p> $y_1(\tau) = T_0 \sum_{k=-\infty}^{\infty} \delta(\tau - kT_0)$	 <p>The same comb function in step 6) should be used here:</p> $Y_1(f) = \sum_{k=-\infty}^{\infty} \delta(f - kf_0)$

(Continued)

Step	Time domain	Frequency domain
12)	<p>$s < 1$</p>  <p>$s = 1$</p>  <p>$s > 1$</p>  $(1/s)\psi(\tau/s)*y_1(\tau) = (T_0/s) \sum_{k=-\infty}^{\infty} \psi(\tau/s)*\delta(\tau - kT_0)$ $= (T_0/s) \sum_{k=-\infty}^{\infty} \psi[(\tau - kT_0)/s]$ <p>Of all of the preceding illustrations, only the first case does not have aliasing.</p>	 <p>Because the sampling resolution in frequency is fixed for all scales, it might be too coarse for some large scales. This can generate aliases in time domain, which can be seen clearly on the left. Therefore, it poses an upper limit in scale such that the aliasing error can be kept within an acceptable limit.</p> $\Psi(sf)Y_1(f) = \sum_{k=-\infty}^{\infty} \psi(skf_0)\delta(f - kf_0)$
13)	 $w_2(\tau) = \frac{\sin(\pi f_1 \tau)}{\pi f_1 \tau} e^{i2\pi f_1 \tau}$ <p>where $f_1 = Nf_0$.</p>	 <p>The window function that truncates the discrete frequencies is:</p> $W_2(f) = \begin{cases} 1 & -\varepsilon < f < f_1 \\ 0 & \text{otherwise} \end{cases}$
14)	<p>$s < 1$</p>  $(1/s)\psi(\tau/s)*y_1(\tau)*w_2(\tau) = (T_0/s)\psi(\tau/s)*[y_1(\tau)*w_2(\tau)]$ $= (T_0/s) \sum_{k=-\infty}^{\infty} \psi(\tau/s)*w_2(\tau - kT_0)$ <p>Compared with the equation in step 12), we notice that here $\psi(\tau/s)$ convolutes with $w_2(\tau - kT_0)$, instead of $\delta(\tau - kT_0)$. This will generate distortions around kT_0.</p>	 $\Psi(sf)Y_1(f)W_2(f) = \sum_{k=0}^{N-1} \Psi(skf_0)\delta(f - kf_0)$ <p>Because the window width is also fixed, $\Psi(sf)$ can be cut off if s is chosen too small. So, it poses a lower limit in scale such that all dilated wavelet bases should have supports within $0 \leq f < f_1$.</p>

Acknowledgments

This research is partially supported by Wang Kuang Cheng Foundation (Hong Kong), Ball Foundation, and the National Basic Research Plan and the project of Innovative Research, Chinese Academy of Science. The authors thank X. B. Cheng for his insightful discussion on amplitude modulation.

References

- ¹Garnier, V. H., Epstein, A. H., and Greitzer, E. M., "Rotating Waves as a Stall Inception Indication in Axial Compressors," *Journal of Turbomachinery*, Vol. 113, April 1991, pp. 290–302.
- ²Day, I. J., "Stall Inception in Axial Flow Compressors," *Journal of Turbomachinery*, Vol. 115, No. 1, 1993, pp. 1–9.

- ³Camp, T. R., and Day, I. J., "A Study of Spike and Modal Stall Phenomena in a Low-Speed Axial Compressor," *Journal of Turbomachinery*, Vol. 120, July 1998, pp. 393–401.

- ⁴Hoying, D. A., Tan, C. S., Vo, H. D., and Greitzer, E. M., "Role of Blade Passage Flow Structures in Axial Compressor Rotating Stall Inception," *Journal of Turbomachinery*, Vol. 121, Oct. 1999, pp. 735–742.

- ⁵Gong, Y., Tan, C. S., Gordon, K. A., and Greitzer, E. M., "A Computational Model for Short-Wavelength Stall Inception and Development in Multistage Compressors," *Journal of Turbomachinery*, Vol. 121, Oct. 1999, pp. 726–734.

- ⁶Tryfonidis, M., Etchevers, O., Paduano, J. D., Epstein, A. H., and Hendricks, G. J., "Prestart Behavior of Several High-Speed Compressors," *Journal of Turbomachinery*, Vol. 117, No. 1, 1995, pp. 62–81.

⁷Bright, M. M., Qammar, H. K., Weigl, H. J., and Paduano, J. D., "Stall Precursor Identification in High-speed Compressor Stages Using Chaotic Time Series Analysis Methods," *Journal of Turbomachinery*, Vol. 119, No. 3, 1997, pp. 491–498.

⁸Lin, F., "Use of Symbolic Time Series Analysis for Stall Precursor Detection," AIAA Paper 98-3310, July 1998.

⁹Liao, S. F., and Chen, J. Y., "Time-Frequency Analysis of Compressor Rotating Stall by Means of Wavelet Transform," American Society of Mechanical Engineers, Paper 96-GT-57, June 1996.

¹⁰Cheng, X. B., "Wavelet Analysis and Stall Precursors of Compressor Rotating Stall" (in Chinese) Ph.D. Dissertation, Inst. of Engineering Thermophysics, Chinese Academy of Sciences, Beijing, People's Republic of China, 2000.

¹¹Le, Dzu K., Owen, A. K., and Mattern, D. L., "Multiscale Analysis of Stall Inception and Instabilities in an Axi-Centrifugal Turboshift Engine," AIAA Paper 96-3174, July 1996.

¹²Inoue, M., Kuroamaru, M., Yashida, S., and Furukawa, M., "Short- and Long-Scale Disturbances Leading to Rotating Stall in an Axial Compressor Stage with Different Stator/Rotor Gaps," American Society of Mechanical Engineers, Paper 2001-GT-341, June 2001.

¹³Höss, B., Leinhos, D., and Fottner, L., "Stall Inception in the Compressor System of a Turbofan Engine," *Journal of Turbomachinery*, Vol. 122, No. 1, 2000, pp. 32–44.

¹⁴Torrence, C., and Compo, G., "A Practical Guide to Wavelet Analysis," *Bulletin of the American Meteorological Society*, Vol. 79, No. 1, 1998, pp. 61–78.

¹⁵Farge, M., "Wavelet Transforms and Their Applications to Turbulence," *Annual Reviews of Fluid Mechanics*, Vol. 24, 1992, pp. 395–457.

¹⁶Nie, C. Q., Xu, G., Cheng, X. B., and Chen, J. Y., "Micro Tip Injection and Its Unsteady Response in a Low-Speed Axial Compressor," *Journal of Turbomachinery*, Vol. 124, No. 4, 2002, pp. 572–579.

Design Methodologies for Space Transportation Systems

Walter E. Hammond

Design Methodologies for Space Transportation Systems is a sequel to the author's earlier text, *Space Transportation: A Systems Approach to Analysis and Design*. Reflecting a wealth of experience by the author, both texts represent the most comprehensive exposition of the existing knowledge and practice in the design and project management of space transportation systems. The text discusses new conceptual changes in the design philosophy away from multistage expendable vehicles to winged, reusable launch vehicles, and presents an overview of the systems engineering and vehicle design process as well as the trade-off analysis. Several chapters are devoted to specific disciplines such as aerodynamics, aerothermal analysis, structures, materials, propulsion, flight mechanics and trajectories, avionics, computers, and control systems. The final chapters deal with human factors, payload, launch and mission operations, and safety. The two texts by the author provide a valuable source of information for the space transportation community of designers, operators, and managers. A CD-ROM containing extensive software programs and tools supports the text.



Contents:

An Overview of the Systems Engineering and Vehicle Design Process ■ The Conceptual Design and Tradeoffs Process ■ Taking a Closer Look at the STS Design Sequence ■ Aerothermodynamics Discipline ■ Thermal Heating and Design ■ Structures and Materials ■ Propulsion Systems ■ Flight Mechanics and Trajectories ■ Avionics and Flight Controls ■ Multidisciplinary Design Optimization ■ Life Support and Human Factors/Ergonomics ■ Payloads and Integration ■ Launch and Mission Operations ■ Related Topics and Programmatic ■ Appendices

AIAA Education Series

2001, 839 pp, Hardcover ■ ISBN 1-56347-472-7

List Price: \$100.95 ■ AIAA Member Price: \$69.95 ■ Source: 945